DOI: 10.15480/882.9317

Eighth International Symposium on Marine Propulsors
smp'24, Berlin, Germany, March 2024

Further development and discrepancy analysis of the acoustic overlapping mesh technique

Youjiang Wang[1,2,*], Zhuangtao Yang[3,4], Zhenghao Liu[5], Tao Zhang[4], Long Yu[1,2]

[1] Key Laboratory of Marine Intelligent Equipment and System, Ministry of Education, Shanghai, China
[2] School of Ocean and Civil Engineering, Shanghai Jiao Tong University, Shanghai, China
[3] School of Marine Science and Technology, Northwestern Polytechnical University, Xi'an, Shaanxi, China
[4] Kunming Branch of the 705 Research Institute, China State Shipbuilding Corporation Limited, Kunming, China
[5] Marine Design and Research Institute of China, Shanghai, China

ABSTRACT

The acoustic overlapping mesh (AOM) technique proposed by the author is extended by clustering CFD cells on solid surfaces. Three causes for the discrepancy between the source level spectrum obtained with the original CFD mesh and the AOM technique are identified and analyzed. The discrepancy from two of the three causes could be controlled by defining the acoustic mesh size correctly. The guidelines for the acoustic mesh size are given theoretically and verified by numerical simulations. The discrepancy from one cause is complicated and needs more investigation. The cavitating Delft twist foil is used as the simulation case. A clear reduction in acoustic evaluation time is observed. Compared to the calculation with the original CFD mesh, the AOM technique could help reduce the computational time by more than 99% while maintaining a spectrum discrepancy of around 1dB.

Keywords

Acoustic Overlapping Mesh, Hydrodynamic Noise, Underwater Radiated Noise, Cavitation, Acoustic Analogy

1 INTRODUCTION

A widely accepted way to calculate the hydrodynamic noise is the hybrid method combining the computational fluid dynamics (CFD) method and the acoustic analogies. For marine propellers, the Ffowcs William Hawkings (FWH) acoustic analogy proposed by William and Hawkings (1969) is thought to be the best choice, as it can consider the moving boundaries. Most experiences are borrowed from the aeroacoustics community. However, the cavitation phenomenon makes the hydrodynamic noise calculation a unique problem. The volumetric sound source or the Lighthill stress tensor term cannot simply be ignored.

Until today, calculating the sound spectrum of underwater radiated noise (URN) from the hydrodynamic simulations efficiently and accurately still remains a problem to solve. The original paper by William and Hawkings (1969) proposed two ways to use the integral form of the FWH acoustic analogy. One way is integrating the sound pressure induced by the solid surface sources and volumetric sources directly, named D-FWH here. The other way is using a permeable data surface enveloping the sound source regions, and applying the Farrasart 1A formula (Farassat 2007) on this surface, named as P-FWH here. In the maritime community, P-FWH is without doubt much more popular than D-FWH, mainly due to the deemed prohibitive computational cost of D-FWH. P-FWH has its own accuracy problems, which have been pointed out by more than one research group (Ge et al 2022, Lidtke et al 2019, Testa 2021).

Wang et al (2022a) proposed a technique called dual mesh technique to reduce the computational cost of D-FWH. To distinguish this technique from existing methods also using the name dual mesh, we named it as the acoustic overlapping mesh (AOM) technique in the following. With the AOM technique, an acoustic mesh that overlaps with the CFD mesh is used to cluster the CFD mesh cells into large groups. Each group is regarded as a single cell when evaluating sound pressures. In the preliminary test case of the cavitating PPTC propeller, it has been shown that this method reduces the computational effort by more than 98% while sacrificing little accuracy. In that work, the AOM technique was only applied to the volumetric sound sources. The integration over the surface became the dominant computational burden because the CFD mesh on the solid surface is usually quite dense. Besides, a systematic and rigorous analysis of the acoustic result discrepancy caused by using the AOM technique is yet to be analyzed.

In the current work, we continued the above-mentioned work by extending the AOM technique to the solid surfaces. The method and the corresponding open-access code are validated on the cavitating hydrofoil case, that is to say, the Delft twist foil case. Besides, preliminary work assessing the influence of acoustic mesh resolution on the acoustic result is also carried out. In section 2, the AOM technique is described briefly together with a theoretical analysis of the discrepancy causes. In section 3, the

computational results are presented and analyzed. In section 4, the main conclusions are drawn.

2 METHODOLOGIES

The AOM technique has been presented in our previous works (Wang et al 2022a, Wang et al 2022b). The FWH acoustic analogy and the AOM technique are also described briefly here for the purpose of completeness. At the end of this section, three causes for the numerical discrepancy of the AOM technique are identified and analyzed theoretically.

2.1 FWH acoustic analogy

The FWH acoustic analogy (Williams & Hawkings 1969) is expressed as a non-homogeneous wave equation about sound pressure p' or density fluctuation ρ'. Its integral formulation provides more convenience for the acoustic evaluation and is adopted in this work. The sound sources are numerically separated into three parts, i.e. thickness, loading and volumetric terms, where the last one is also called the Lighthill stress tensor. The sound pressure induced by thickness, loading, and volume terms are denoted as p'_T, p'_L, and p'_V, respectively, which implies

$$p' = p'_T + p'_L + p'_V. \tag{1}$$

The integral formulations for surface terms p'_T and p'_L are widely known as Farassat 1A formulation (Farassat 2007):

$$p'_T = \frac{1}{4\pi}\int_{f=0}\left[\frac{\rho_0\left(\dot{U}_n + U_{\dot{n}}\right)}{r(1-M_r)^2}\right]_{\text{ret}} \mathrm{d}S + \frac{1}{4\pi}\int_{f=0}\left[\frac{\rho_0 U_n\left[r\dot{M}_r + c_0(M_r - M^2)\right]}{r^2(1-M_r)^3}\right]_{\text{ret}} \mathrm{d}S \tag{2}$$

$$p'_L = \frac{1}{4\pi c_0}\int_{f=0}\left[\frac{\dot{L}_r}{r(1-M_r)^2}\right]_{\text{ret}} \mathrm{d}S + \frac{1}{4\pi}\int_{f=0}\left[\frac{L_r - L_M}{r^2(1-M_r)^2}\right]_{\text{ret}} \mathrm{d}S + \frac{1}{4\pi c_0}\int_{f=0}\left[\frac{L_r\left[r\dot{M}_r + c_0(M_r - M^2)\right]}{r^2(1-M_r)^3}\right]_{\text{ret}} \mathrm{d}S \tag{3}$$

where

$$U_i = v_i + \rho/\rho_0(u_i - v_i) \tag{4}$$

$$L_i = pn_i + \rho u_i(u_n - v_n) \tag{5}$$

In Equations (2)-(5), f is a continuous field function to define the sound source surfaces, i.e. $f < 0$, $f = 0$, and $f > 0$ mean positions inside, on, and outside the surface, respectively; c_0 is the sound speed; ρ is the local density; ρ_0 is the undisturbed density; v and u are surface motion velocity and flow velocity, respectively; the subscript i means components of vector and n means normal to surface; the other subscripted variables denote dot products of a vector and a unit vector implied by the subscript, except $L_M = L_i M_i$ whereby M_i presents the vectorial Mach number, i.e. $M_i = v_i / c_0$; r_i is a vector from the source point to observer position, r is its length, and n_i is the unit normal vector on the surface directing into the fluid domain; the dot over a variable means time derivative; the subscript ''ret'' means that variables inside the square brackets are computed at the corresponding retarded time, i.e. at $\tau = t - r / c_0$.

The integral formulation for volume term p'_V can be expressed as

$$p'_V = \frac{1}{4\pi c_0^2}\int_{f>0}\left[\frac{\hat{r}_i\hat{r}_j\ddot{T}_{ij}}{r}\right]_{ret} dV + \frac{1}{4\pi c_0}\int_{f>0}\left[\frac{\left(3\hat{r}_i\hat{r}_j - \delta_{ij}\right)\left(r\dot{T}_{ij} + T_{ij}\right)}{r^3}\right]_{ret} dV \tag{6}$$

where c_0, f, r_i, r have the same meanings as that for Equations (2)-(5), $\hat{r}_i$ is the unit vector in the direction of r_i; δ_{ij} is the identity tensor, T_{ij} is the Lighthill stress tensor. The Lighthill stress tensor is given by Lighthill (1954) as

$$T_{ij} = \rho u_i u_j - \tau_{ij} + \left(p' - c_0^2\rho'\right) \tag{7}$$

where u_i is the flow velocity, τ_{ij} is the viscous stress tensor, p' and ρ' are deviations from the uniform reference state of pressure p_0 and density ρ_0. Normally, the second term and third term on the right-hand side of Equation (7) are negligible compared to the first term. However, for cavitating flow, the local density variation makes the third term significant and shows the property of a monopole sound source (Wang et al. 2022a).

2.2 The acoustic overlapping mesh technique

The core idea of the AOM technique is to use an acoustic mesh that is much coarser than the CFD mesh to cluster the CFD cells into groups. All CFD cells whose center is in the same acoustic mesh cell are clustered as one group, as shown in Figure 1. Each group is regarded as a single cell when evaluating sound pressures. The important thing is then the determination of the sound source terms (e.g. U_i, L_i, T_{ij}) for each cell group. The objective when developing the method is to keep the difference between acoustic results obtained with CFD cells and the acoustic mesh as small as possible.

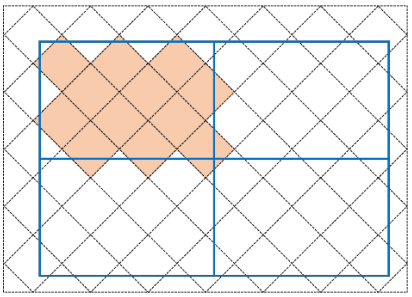

Figure 1. The AOM technique concept. The dashed black lines represent the CFD mesh and the solid blue lines represent the acoustic mesh. The shading area depicts the CFD cells being clustered to one group corresponding to the upper-left acoustic mesh cell.

To reduce the influence of the acoustic mesh, the integrals of the sound source terms should be kept constant. For that purpose, the quantities for each cell group are calculated as the volume- or area-weighted average of the original quantities on the CFD mesh. For the volumetric sound source terms, the unified formula is

$$\phi_{G_k} = \frac{\sum_{i \epsilon G_k} \phi_i V_i}{V_{G_k}} \quad (8)$$

where ϕ_{G_k} denotes a variable value for the k-th cell group; $i \epsilon G_k$ means all CFD cells that belong to the k-th group; ϕ_i and V_i denote the variable value and volume of corresponding CFD cells, respectively; V_{G_k} is the volume for the k-th group. V_{G_k} can be the cell volume of acoustic mesh or the sum of the volume of all CFD cells belonging to the current group (i.e. $V_{G_k} = \sum_{i \in G_k} V_i$). The important thing is that it should be the same when calculating ϕ_{G_k} and when evaluating sound pressures numerically with Equation (6). The variables to be calculated include the position (or center) and the Lighthill tensor T_{ij}.

For the surface sound source terms, the unified formula is

$$\phi_{G_k} = \frac{\sum_{i \epsilon G_k} \phi_i S_i}{S_{G_k}} \quad (9)$$

where S_i and S_{G_k} denote the area for CFD face cell and the k-th group, respectively. Because volumetric acoustic mesh is used to cluster the CFD face cells, for S_{G_k} we can only use the sum of the CFD face cell area, i.e. $S_{G_k} = \sum_{i \in G_k} S_i$. The variables to be calculated includes the position (or center), the thickness term U_n, the loading term L_i, and the moving velocity v_i.

2.3 Source of discrepancy

The AOM technique clusters the CFD cells into large groups. Each group has only one unique center and one value for every sound source term. Thus, it is inevitable that some detailed information on the CFD mesh will be lost, which results in numerical discrepancies between the sound pressures evaluated with the CFD mesh and the AOM technique. Three sources of discrepancy are identified in this section and the upper limits of the discrepancy are analyzed.

Cause I: The phase difference due to the change of distance *r*. On the straight line drawn through the observer and the cell group center, the distance change could be as large as $\pm h/\sqrt{2}$, where h is the cell size of the acoustic mesh. The phase angle discrepancy could thus be $\alpha = 2\sqrt{2}\pi h/\lambda$, which happens for two sound sources whose distances to the observer change from $r_G + h/\sqrt{2}$ and $r_G - h/\sqrt{2}$ to r_G, where r_G is the distance of the group center to the observer. For the worst case, two perfectly cancelling signals will now generate some noise or vice versa. In this case, the change factor is infinite or zero, with the change factor being defined as

$$C_I = \frac{p'_{AM}}{p'_{CFD}} \quad (10)$$

where p'_{AM} and p'_{CFD} are the sound pressures obtained with the acoustic mesh and CFD mesh, respectively.

We can see that, the discrepancy depends on acoustic mesh size h, wave length λ, and also the distribution of sound sources. Theoretically, the discrepancy has no upper limit. Statistically, it could have an upper limit with regards to h/λ. This aspect needs analysis of various practical cases.

Cause II: The sound pressure magnitude difference due to the change of distance r. The distance r is in the denominator for each term in Equations (2), (3), and (6). The distance could change from $r_G \pm h/\sqrt{2}$ to r_G. The sound pressure magnitude changing factor is then

$$C_{II} = \frac{r^n}{\left(r \pm \frac{h}{\sqrt{2}}\right)^n} = \frac{1}{\left(1 \pm \frac{h}{\sqrt{2}r}\right)^n} \quad (11)$$

where n could be 1 or 2, depending on the exponent of r in the dominant term in Equations (2), (3), and (6).

Cause III: The change of direction $\hat{r}_i$, which influences L_r and M_r. The maximum angle between the old and new $\hat{r}_i$ could be

$$\beta = tan^{-1}\left(\frac{h/\sqrt{2}}{r}\right) \quad (12)$$

The worst case is that the angle between L_i *or* M_i and $\hat{r}_i$ changes from $\pi/2$ to $\pi/2 \pm \beta$ or vice versa. In this case, the change factor C_{III} could be infinitive or zero.

The discrepancy from Cause II and III both depends on the ratio h/r or r/h. For a given distance and the requirement of discrepancy, we can find a corresponding requirement on h to control the discrepancy resulting from Cause II.

As an example, for cavitating noise, Cause III has no effect. To ensure that the Sound Power Level (SPL) discrepancy resulting from Cause II is less than 1dB or 0.1dB, we should have *r/h* > 6.5 or *r/h* > 62, respectively.

3 RESULTS AND DISCUSSION

The numerical results of a cavitation simulation and acoustic evaluations about the Delft twist foil are presented here. Analysis is carried out focusing the discrepancy and computational time of the AOM technique.

3.1 Numerical Setups

The AOM technique has been implemented as an acoustic analogy library name libAcousticPlus for the open source CFD solver OpenFOAM. The solver interPhaseChangeFoam in OpenFOAM is used to obtain the transient cavitating flow field around the Delft twist foil. This hydrofoil has a chord length of 150mm, and is twisted so that it has a larger angle of attack in the middle than in the tip. For the simulated case, the foil has an angle of attack of -2 degrees and the inflow velocity is 6.97m/s. The pressure on the outlet is 29kPa and the saturated vapor pressure is 2.97kPa. Thus, the cavitation number is 1.07.

As shown in Figure 2, the computational domain extends 2c ahead of the leading edge and 4c behind the trailing edge, where c is the chord length. The cross-section has a size of 0.15m x 0.3m. The symmetrical condition is used in the middle plane. The details for the CFD mesh are listed in Table 1 and the CFD mesh is depicted in Figure 3. The $k-\omega$ SST IDDES model is adopted as the turbulence model and the Schnerr-Sauer model is used to model the mass transfer for cavitation. As for numerical schemes, the second-order upwind scheme is used for the convection of velocity and turbulence kinematic energy *k*. First order

upwind scheme is used for the convection of the variable ω. The second-order implicit scheme called backward is used for the temporal advancing and the central difference scheme is used for the diffusion term. In the PIMPLE scheme, 5 outer correction iterations and 3 inner correction iterations are used. The dynamically adjustable time step with the max Courant number being 10 is applied.

In (Wang 2023) an analysis of the numerical setups on the cavitating simulation result has been discussed. It was concluded that with the current setups the hydrodynamic results are not sensitive to the setups, except for the mesh. Further refinement might be necessary, but a realistic transient cavitating flow can already be obtained.

For the acoustic evaluation, totally 360 observers are arranged on the symmetry plane (xz plane with y=0.15m). The observers are placed on ten circles having the same center with the hydrofoil and different radii. The radii determine the distance of observers to the foil and have the values of 1.5c, 2c, 4c, 8c, 16c, 32c, 64c, 100c, 200c, and 400c, where c is the foil's chord length. On each circle 36 observers are placed with a circumferential interval of 10 degrees. The angular direction of 0 degree means straight downstream, and 90 degrees mean vertical upward. A

Table 1. Details of the CFD simulation mesh

description	value
cell size on leading edge	1.0 mm
cell size on tunnel walls	10 mm
number of nodes for the chord	235
first cell height on the foil	5e-3mm
expansion rate for prism layers	1.2
y+ value on the foil	≈ 1
total number of cells	3.4M

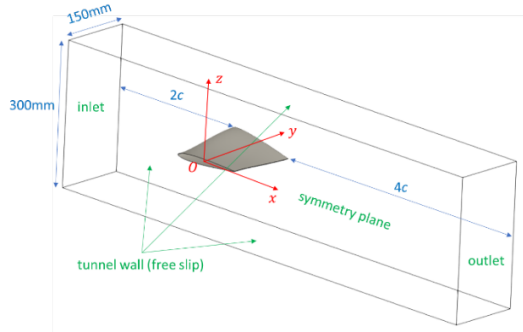

Figure 2. The computational domain for the cavitating simulation and the coordinate system.

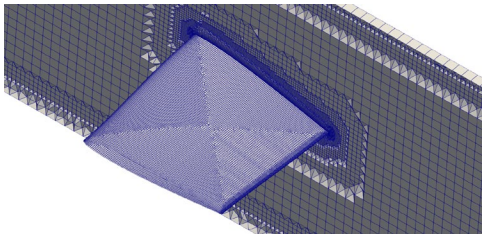

Figure 3. The computational mesh for the cavitating simulation.

cubic box having the size of $2c \times c \times c$ is used as the sound source region, with 0.5c upstream of the leading edge and 0.5c downstream of the trailing edge. It has been checked that all cavities are included in this box. The sound speed is set as 1450 m/s.

For the AOM technique, two different acoustic meshes with cell size being h=c and h=c/15 are used. They are depicted in Figure 4 and named as AM h=c and AM h=c/15 in the following text. The cell groups formed on the hydrofoil surface with AM h=c/15 are shown in Figure 5. Compared with the CFD surface cells in Figure 3, the AOM technique reduces the number of cells to be integrated for acoustic evaluations.

3.2 Cavitation simulation

A steady RANS simulation without cavitation is firstly carried out. Then the transient simulation is conducted with the $k-\omega$ SST IDDES model and cavitation model being turned on. When a clear periodic phenomenon is achieved, the transient simulation was run for another one second of physical time to gather data for the acoustic evaluation. A visual comparison of the cavity shape with the experiment is given in Figure 6. The shedding frequency obtained by analyzing the cavity volume variation is 31Hz, which means the one second duration for the acoustic evaluation consists of around 31 cavity shedding cycles. Other results regarded to the hydrodynamic analysis can be found in (Wang 2023).

3.3 Acoustic evaluation with CFD mesh

The acoustic results evaluated with the original CFD mesh is used as the benchmark data. This data is analyzed here to get knowing properties of the noise including the decay rate and the dominant component.

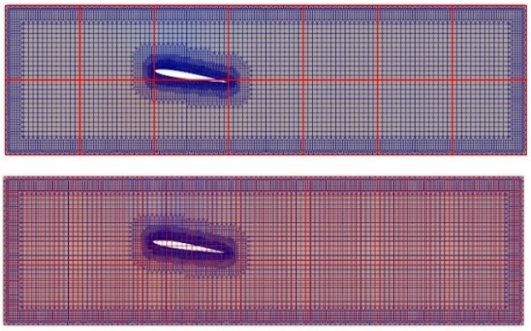

Figure 4. The acoustic meshes (red lines) with the CFD mesh (blue lines) in the background. Up: AM h=c, down: AM h=c/15.

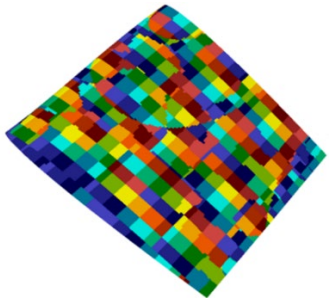

Figure 5. The cell groups on the foil surface obtained with acoustic mesh h=c/15. Each colored block is a cell group.

The following formula is normally used to calculate the source level of URN,

$$SL = SPL(r) + 20\log(r). \quad (12)$$

There is a distance threshold for the application of Equation (12). This is because, due to the different phase angle offset for different distances, the distance should be large for sound pressure to have a r^{-1} decay rate. Over this threshold, we call it the r^{-1} varying range. This can be reflected in the difference between SLs calculated with SPL at different positions, as shown in Figure 7.

We use the SL obtained with the farthest position as the standard value, and use the maximum ΔSL over all frequencies to determine if the current distance is enough to calculate the converged SL. We can also get the distance threshold value in this way when defining a maximum SL deviation. It is found that the threshold distance varies with direction, as shown in Figure 8. When the max allowed deviation is 1dB, the threshold distance is around 20c; while it is a little less than 120c for 0.1dB.

The surface noise (the noise evaluated by only considering FWH integration on solid surfaces) has been calculated alone. Its comparison with the total noise (the noise evaluated by considering FWH integration both on solid surfaces and in fluid domains) is given in Figure 9 for both near field and far field. It is evident that the surface noise is by far weaker than then total noise, and the volumetric noise is the dominant one in the total noise. Thus, the property and discrepancy of the total noise represent those of the volumetric noise (or cavitating noise). To study the surface noise, one needs special analysis. In the way of turning off the volumetric sound source, we isolated the surface noise and also investigate the property and discrepancy regarding it.

The SL of surface noise changes more with the distance than the total noise, as shown in Figure 10. The threshold distance is also larger. This is because there is a loading term that generates sound pressure being proportional to r^{-2}. When this term is dominant among surface noise sources, the decay rate is r^{-2}. As it is overpassed by other terms when the distance increases, the surface noise reaches the r^{-1} varying range. For a maximum allowed deviation of 1dB, the threshold distance is around 180c, and it is 360c for 0.1dB. These values should be seen with cautions, because the maximum distance we have is only 400c. It is very probable that even 400c is not enough for the surface noise to enter the r^{-1} varying range.

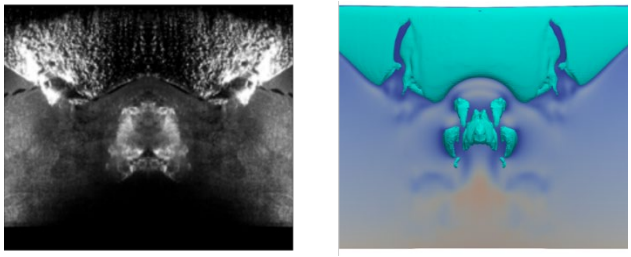

Figure 6. Comparison of the simulated cavity shape with the experiment observation (van Terwisga 2010) for one instant in time.

3.4 Total Noise Discrepancy with AOM technique

In section 3.4 and 3.5, we focus on the discrepancy between the source level spectrums obtained with the original CFD mesh and the AOM technique. As the cavitating noise is dominant in the total noise, the conclusions regarding the total noise can direct apply to the cavitating noise.

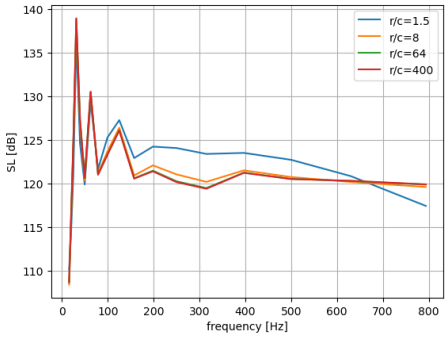

Figure 7 SLs calculated with SPL at different distances.

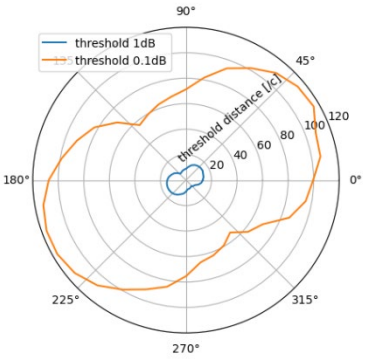

Figure 8. The threshold distance for r^{-1} varying range.

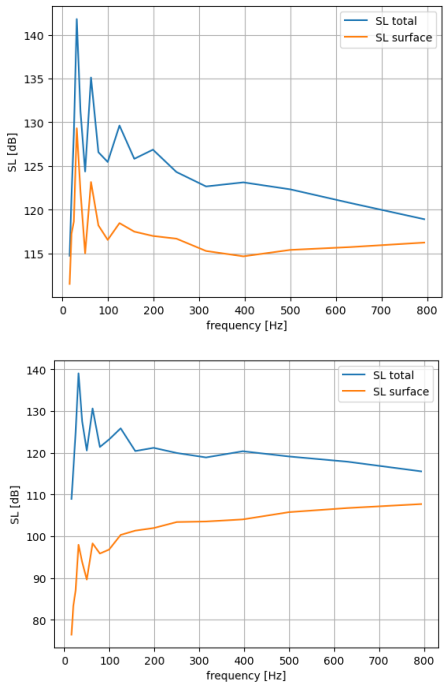

Figure 9. Comparison of total noise and surface noise for r/c = 1.5 (upper) and r/c = 400 (lower).

The discrepancy varies with frequency, distance, and angular direction. In Figure 11 the SL spectra obtained with different acoustic meshes are shown. The discrepancy varies with frequency, and the coarser acoustic mesh (h=c) leads to larger discrepancy than the finer acoustic mesh (h=c/15).

The maximum discrepancy over all frequencies is used to represent the discrepancy for each observer position. In Figure 12, the variation of maximum discrepancy with direction is shown for different distances and acoustic meshes. The trend is that the discrepancy is larger in the direction with 0 degree and 180 degrees. This could be due to the fact that the cavity structure has the largest dimension along the x direction, and needs more refinement to capture sound source details. This assumption would be validated with an anisotropic acoustic mesh in the future.

The maximum discrepancy over all directions on the same circle is used to represent the discrepancy for the specific distance. Figure 13 shows the variation of maximum discrepancy with distance. The maximum discrepancy firstly decreases with the distance, and then remains constant as the distance increases further. The discrepancy decreasing with distance is mainly attributed to Cause II with the exponent n being 1. The conclusions obtained with theoretical analysis in section 2.3, which state that r/h > 6.5 ensures that the discrepancy is less than 1dB, and r/h > 62 ensures that the discrepancy is less than 0.1dB, are verified in Figure 13.

Along the direction with 0 degree, the discrepancy spectra for different observers are shown in Figure 14. Decrease of the discrepancy with distance when r is less than the critical value can be observed. Besides, when r is larger than the critical value, the discrepancy spectrum also keeps almost constant. This remaining discrepancy is attributed to Cause I, and it is observed that it increases with frequency.

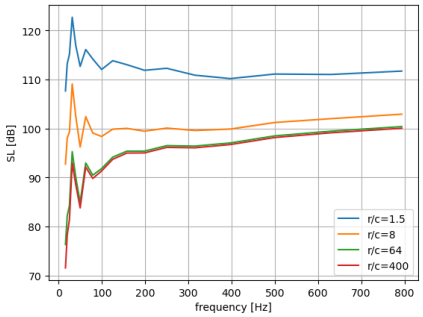

Figure 10. SLs of surface noise calculate with SPL at different distances.

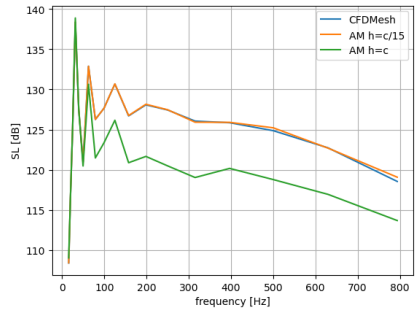

Figure 11. Source level spectra obtained with different acoustic meshes for the observer having r/c=1.5 and angle direction of 0.

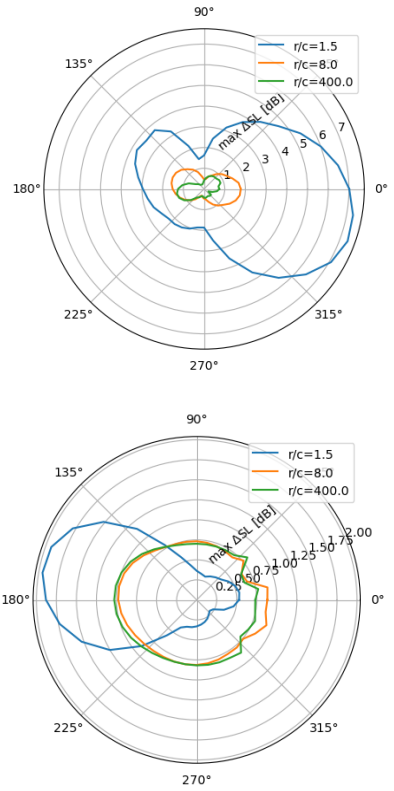

Figure 12. Variation of maximum discrepancy with direction. Up: AM h=c, down: AM h=c/15.

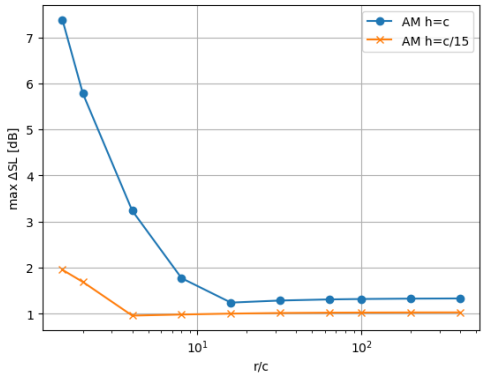

Figure 13. Variation of maximum discrepancy with distance.

3.5 Surface Noise Discrepancy with AOM technique

The surface noise in the current work includes only the loading term as the foil does not move or deform. The variation of maximum discrepancy with distance is shown in Figure 15. The trend is the same with the total noise, i.e. the maximum discrepancy decreases with distance in the near field and becomes independent of the distance in the far field. In the near field, the discrepancy can be attributed mainly to Cause II and Cause III, which has clear relationship with the distance r. If the r-independent

discrepancy is excluded, a rough estimation is that r/h>50 ensures that this part of discrepancy less than 1dB.

In the far field the maximum discrepancy becomes almost constant when the distance varies. This remaining discrepancy is attributed to Cause I. The coarse acoustic mesh might smear out small scale pressure variations on the foil surface induced by moving vorticity or cavity structures. This could be improved by refining the acoustic mesh near the surface and along the streamwise direction.

Figure 15 shows the directivity of the maximum discrepancy. With AM h=c, the largest discrepancy occurs in the direction around 165 and 345 degrees. This aligns with the hydrofoil chord direction in the middle plane. In this direction, Cause I and Cause II has a larger effect than other directions. In other directions, the hydrofoil size is small, the distance change is limited. With AM h=c/15, the maximum discrepancy happens around 0 and 180 degrees due to the similar reason.

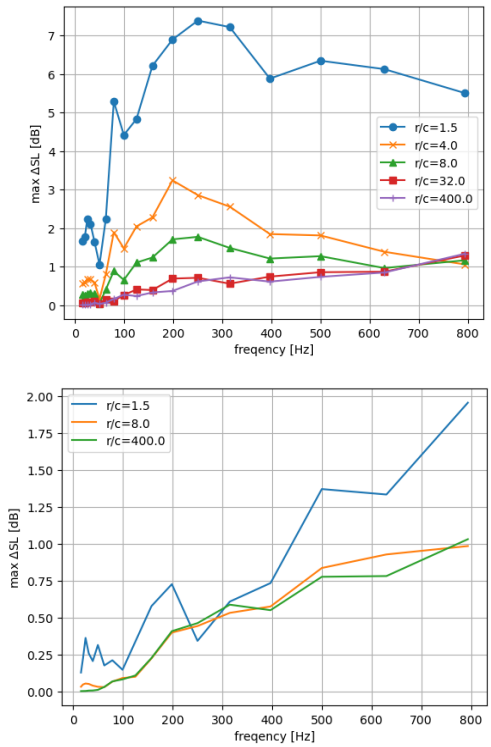

Figure 14. Variation of discrepancy with frequency for observers with different distances along the 180 degree direction. Up: AM h=c, down: AM h=c/15.

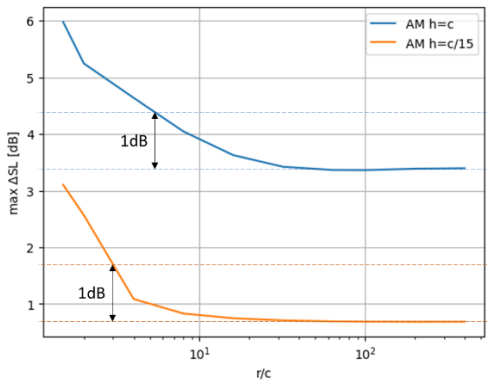

Figure 15. Variation of maximum surface noise discrepancy with distance.

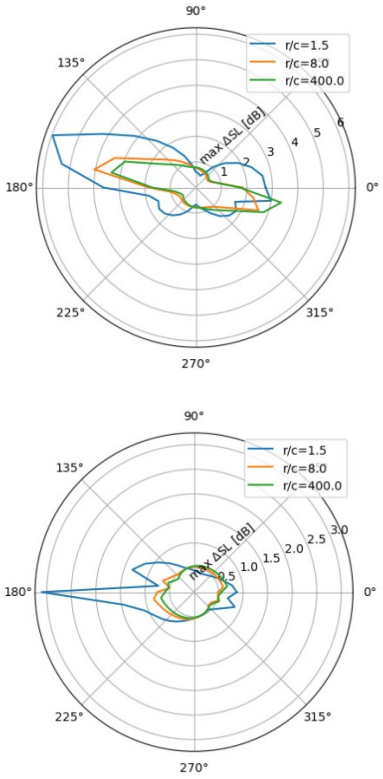

Figure 16. Variation of maximum surface noise discrepancy with direction. Up: AM h=c, down: AM h=c/15.

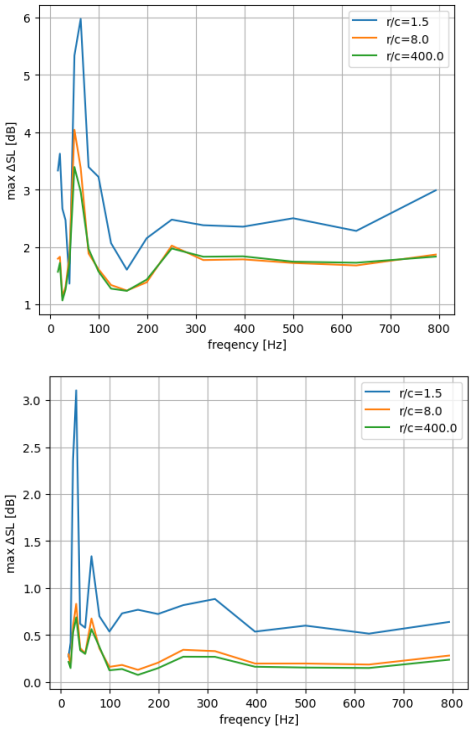

Figure 17. Variation of surface noise discrepancy with frequency for observers with different distances. Up: AM h=c, along the direction of 160 degrees; down: AM h=c/15, along the direction of 180 degrees.

The discrepancy spectra for observers with different distances are shown in Figure 17. When *r* is larger than the critical value, the discrepancy spectrum keeps almost constant. However, the discrepancy does not show an increase with frequency as for the total noise. This part of discrepancy is attributed to Cause I and needs more investigation in the future.

3.5 Acoustic Evaluation Time

The acoustic evaluations are conducted for the physical time of 1s with time step being 0.0005s, which means totally 2000 timesteps. The computational time for each acoustic evaluation is listed in Table 2 for the comparison purpose. With ability to keep the far-field maximum discrepancy for the spectrum within 1.1dB, the acoustic mesh h=c/15 reduces the computational time from 54K seconds to 220 seconds by 99.5%.

Table 2. Acoustic evaluation time for different cases.

evaluation case		cell number	comp. time
total noise	CFD mesh	3.4M	54,244s
	AM h=c/15	49.5K	220s
	AM h=c	14	100s
surface noise	CFD mesh	32.4K	69.2s
	AM h=c/15	725	6.78s
	AM h=c	4	5.16s

6 CONCLUSIONS

The acoustic overlapping mesh (AOM) technique is applied to evaluate the noise radiated from the cavitating Delft twist foil. The FWH acoustic analogy with direct volumetric integration is applied, and the AOM technique helps reduce the computational time to an affordable level. A clear reduction of acoustic evaluation time is observed. Compared to the calculation with the original CFD mesh, the AOM technique could help reduce the computational time by more than 99% while maintaining a spectrum discrepancy around 1dB.

The discrepancy between the source level spectrum obtained with the original CFD mesh and the AOM technique are analyzed in details. Three causes named Cause I, II, and III are identified theoretically.

Cause II and Cause III are related to the ratio of distance to acoustic cell size r/h. The discrepancy induced by Cause II could be limited by choosing the suitable acoustic mesh size with a given distance. For the volumetric noise, Cause III has no effect, and r/h > 6.5 ensures that the discrepancy from Cause II is less than 1dB. For the surface noise, a rough estimation is that r/h > 50 can achieve the same effect.

Cause I is related to the ratio of cell size to wave length h/λ and the sound sources distribution. There is no theoretical upper limit for this part of discrepancy. Refining the acoustic mesh helps reduce this part of discrepancy. With the acoustic mesh h=c/15, this discrepancy can be a little larger than 1dB for the volumetric noise and it is less than 1dB for the surface noise. Anisotropic acoustic mesh and local refinement could be a solution to control the computational time and reduce this discrepancy at the same time. This aspect needs further investigations in the future.

It has also been observed that the discrepancy has directivity. Using anisotropic acoustic mesh considering the shape of main sound source region might help to reduce this directivity effect. In the future, investigations will be conducted to find a good strategy for generating acoustic mesh to reduce the discrepancy caused by Cause I and the discrepancy directivity.

ACKNOWLEDGEMENT

This work is supported by National Natural Science Foundation of China (Grant No. 52301377), Natural Science Foundation of Shanghai (Grant No. 23ZR1433800), and the Fundamental Research Funds for the Central Universities. The authors are grateful for these supports.

REFERENCES

Farassat, F. (2007), Derivation of Formulations 1 and 1A of Farassat, Technical Report NASA/TM-2007-214853, NASA, Langley Research Center, Hampton, Virginia, USA, 2007.

Ge, M., Svennberg, U., & Bensow, R. E. (2022). Investigations on prediction of ship noise using the FWH acoustic analogy with incompressible flow input. Ocean Engineering, 257(June), 111531.

Lidtke, A. K., Lloyd, T. P., & Vaz, G. (2019). Acoustic modelling of a propeller subject to non-uniform inflow, Proceedings of SMP'19. Rome, Italy.

Testa, C., Porcacchia, F., Zaghi, S. & Gennaretti M. (2021). Study of a FWH-based permeable-surface formulation for propeller hydroacoustics, Ocean Engineering 240: 109828.

van Terwisga, T. (2010). Explanation with the experimental data for the delft twist 11 foil test case. URL http://maritimetechnology.tudelft.nl/SHS/.

Wang, Y., Göttsche, U., & Abdel-Maksoud, M. (2020). Sound field properties of non-cavitating marine propellers, Journal of Marine Science and Engineering 8: 885.

Wang, Y., Mikkola, T. & Hirdaris, S. (2022a). A fast and storage-saving method for direct volumetric integration of FWH acoustic analogy. Ocean Engineering. 261:112087.

Wang, Y., Mikkola, T. & Hirdaris, S. (2022b). Hydroacoustic evaluation of cavitating flow based on direct FWH approach and dual mesh technique. Proceedings of SMP'22. Wuxi, China.

Wang, Y. (2023). On suitable CFD setups for cavitation dynamics. IOP Conference Series: Materials Science and Engineering. 1288 (1):012053.

Williams, J. F. & Hawkings, D. L. (1969), Sound generation by turbulence and surfaces in arbitrary motion, Phil. Trans. R. Soc. Lond. A 264:321–342.